

See discussions, stats, and author profiles for this publication at: <https://www.researchgate.net/publication/263948960>

Ionic Liquids Confined in a Realistic Activated Carbon Model: A Molecular Simulation Study

ARTICLE *in* THE JOURNAL OF PHYSICAL CHEMISTRY C · JANUARY 2014

Impact Factor: 4.77 · DOI: 10.1021/jp408617j

CITATIONS

11

READS

27

3 AUTHORS, INCLUDING:



[Nav Nidhi Rajput](#)

Lawrence Berkeley National Laboratory

19 PUBLICATIONS 113 CITATIONS

SEE PROFILE



[Joshua David Monk](#)

AMA Inc., Nasa ames research center

35 PUBLICATIONS 438 CITATIONS

SEE PROFILE

Ionic Liquids Confined in a Realistic Activated Carbon Model: A Molecular Simulation Study

Nav Nidhi Rajput,^{†,‡,⊥} Joshua Monk,^{†,§,⊥} and Francisco R. Hung^{*,†,||}

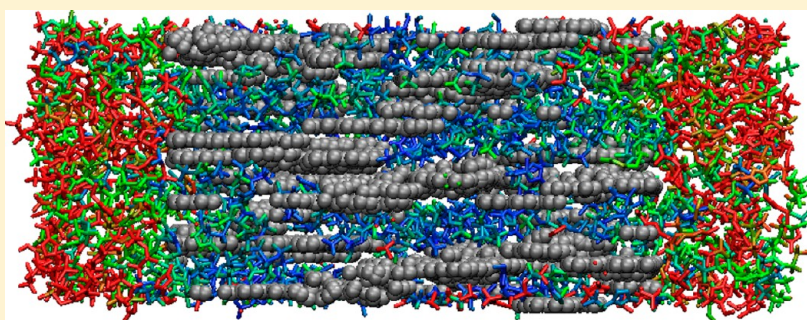
[†]Cain Department of Chemical Engineering, Louisiana State University, Baton Rouge, Louisiana 70803, United States

[‡]Electrochemical Technologies Group, Lawrence Berkeley National Laboratory, Berkeley, California 94720, United States

[§]Thermal Protection Materials Branch, NASA Ames Research Center, Moffett Field, California 94035, United States

^{||}Center for Computation and Technology, Louisiana State University, Baton Rouge, Louisiana 70803, United States

S Supporting Information



ABSTRACT: Classical molecular dynamics simulations were performed to study the structure and dynamics of the ionic liquid (IL) [emim⁺][NTf₂⁻] inside a slit graphitic nanopore and a realistic model of a coconut shell activated carbon (CSAC), which was generated using a reverse Monte Carlo protocol and matches the experimental radial distribution function from the real adsorbent. The CSAC model material consists of semigraphitic carbon sheets with different sizes and shapes, which form irregularly connected pores of roughly rectangular shape. In general, the ions inside the CSAC model material form layers parallel to the walls, as observed for the IL inside slit pores; however, the distribution of pore sizes and the complex pore geometry of the CSAC model materials cause the density profiles and the orientation of the ions to depart significantly from the uniform behavior observed for these properties of the IL inside slit pores. The presence of interconnected pores with a distribution of sizes in the CSAC model materials also causes confinement effects to be weaker than in slit pores of the same size; as a result, the ions inside CSAC model materials have a liquid structure similar to that of the bulk IL and have faster dynamics than those of ions inside slit pores of the same size. The ions near the pore walls of the CSAC model material move slower than the ions that are farther away from the walls, as observed for the IL inside slit pores; however, the complex pore geometry and variations of pore size with position within the CSAC model material cause the dynamics of the confined IL to exhibit significant spatial heterogeneities and depart significantly from the uniform, regular behavior observed in slit nanopores. Our results suggest that the structure and dynamics of ILs confined inside porous materials having heterogeneities in pore size, pore shape, and pore interconnectivity can depart significantly from the properties of ILs confined inside ideal pores of simple geometries.

1. INTRODUCTION

A fundamental understanding of the properties of ionic liquids (ILs) inside nanopores is relevant for their applications in energy storage devices such as electrochemical double layer capacitors (EDLCs).^{1–9} Several groups^{9–18} have attempted to use ILs and their mixtures with solvents as alternative electrolytes in EDLCs, motivated by their excellent thermal stability, nonvolatility, high ion density, and wide electrochemical window. A fundamental understanding of the properties of ILs inside nanopores is also relevant for applications other than EDLCs. For example, ILs have been used recently in the development of ionogels,^{19–23} a new class of hybrid materials involving a solidlike network formed by immobilizing ILs within nanoporous solids (e.g., carbon

nanotubes, porous silicas, organic gelators, polyethylene oxide, cellulose, etc.). Ionogels have potential applications as solid electrolyte membranes in lithium batteries, fuel cells, and DSSCs.^{19–23} Furthermore, the encapsulation of functional molecules into the immobilized IL phase can impart the ionogels with useful properties for potential applications in optics, catalysis and biocatalysis, drug delivery, and sensing and biosensing.^{19–23} In addition, solidification of ILs inside templating nanoporous materials (e.g., carbon nanotubes, templated mesoporous silicas, anodic alumina membranes) is

Received: August 28, 2013

Revised: December 30, 2013

Published: January 2, 2014



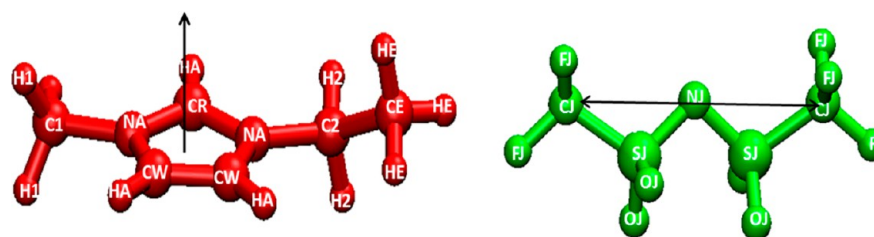


Figure 1. Schematic representation of the IL $[\text{emim}^+][\text{NTf}_2^-]$. The labels are the atom notations used in this work.

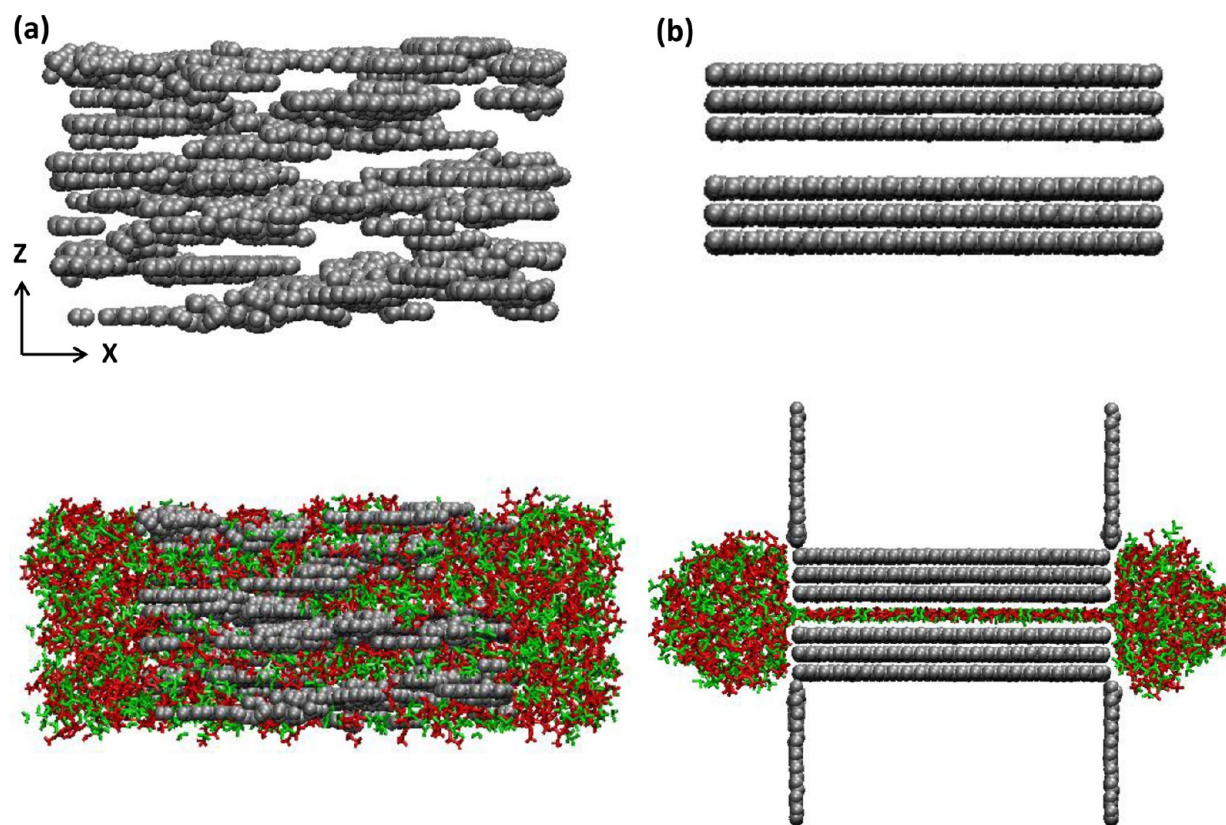


Figure 2. (Top panel) Front views of (a) CSAC model, average pore size $H = 0.75$ nm, and (b) slit graphitic pore, size $H = 0.75$ nm. (Bottom panel) Representative simulation snapshots of the model systems studied, $H = 0.75$ nm and $T = 333$ K. Carbon atoms in the walls are depicted in gray; cations and anions are depicted in red and green.

one step in the synthesis of optically active (fluorescent) and magnetic nanomaterials based on ILs.^{24–30} These IL-based nanomaterials (dubbed “GUMBOS”, for Group of Uniform Materials Based on Organic Salts) hold enormous promise, as they share the inherent functionality and highly tunable properties of ILs,^{31,32} and can be prepared via simple procedures.^{24–30} For example, the Warner group recently synthesized fluorescent 1D-nanomaterials (e.g., nanorods, nanotubes, and nanowires) based on organic salts,²⁹ by introducing these compounds inside anodic alumina membranes; 1D-nanoGUMBOS with diameters between 20 to 500 nm and lengths of 1 to 20 μm have been synthesized. Possible applications of these organic salts-based nanomaterials are envisioned in fields as diverse as optoelectronics, photovoltaics, separations, analytical chemistry, and biomedicine.

The macroscopic performance of IL-based EDLCs is determined by the structural arrangement of the ions, as well as the mobility and electrical properties of the IL confined inside the charged and uncharged nanoporous electrodes. Furthermore, the macroscopic properties of ionogels and

nanoGUMBOS are determined by the structural and dynamical properties of the IL confined inside the nanopores, which are usually uncharged in these materials. Molecular simulations, in close interplay with experiments, are well positioned to provide such fundamental understanding. Recent simulation and theoretical studies have focused on ILs and molten salts confined inside “ideal” nanopores of simple geometry, i.e., slitlike and cylindrical.^{33–73} Although these studies have provided important insights about the properties of the electrical double layer in confined ILs, ideal pore models typically neglect effects of heterogeneities in pore shape, size, and surface roughness, which are present in real nanoporous materials. Recent simulation studies^{74–81} suggest that the effect of such heterogeneities can be important. Curvature effects were observed to significantly affect the capacitance of ILs in onionlike carbons.^{80,81} Recent studies^{74,75} suggest that the capacitance can be improved by carefully tuning the morphology of the electrode surface. Similarly, the properties of ILs inside materials such as CMK-3 mesoporous carbon⁷⁹ and carbide-derived porous carbon,⁷⁶ which exhibit intercon-

nected pores and significant curvature in the pore walls, were observed to be substantially different from the properties of ILs confined inside pores of simple geometry such as slitlike and cylindrical. Furthermore, gas adsorption measurements are typically used to determine the pore size distributions of adsorbents; however, in this analysis it is usually assumed that the material consists of a collection of pores of ideal geometry (slit, cylindrical, spherical) but with a distribution of pore sizes. A recent simulation study⁸² points at the deficiencies of such an assumption in capturing the adsorption behavior in real nanoporous carbons, which typically have heterogeneities in pore shape, pore size, and surface roughness. One fundamental question that remains to be answered is how heterogeneities in pore size, shape, and surface roughness affect the structural and dynamical properties of the IL inside the nanoporous materials. These heterogeneities ultimately affect macroscopic properties in EDLCs such as the capacitance and electrical resistance, as well as the properties of ionogels and IL-based nanomaterials.

In this work we studied the structure and dynamics of a typical IL, [emim⁺][NTf₂⁻], confined inside two model porous carbon materials, a slit graphitic nanopore and a realistic model of a coconut shell activated carbon (CSAC) developed by Pikunic et al.^{83,84} This model was generated using a reverse Monte Carlo simulation protocol in a way that the model material matches the experimental radial distribution function $g(r)$ of a CSAC. This model exhibits semigraphitic carbon sheets with different sizes and shapes, which form irregularly connected pores of roughly rectangular shape. Porous carbons are often derived from coconut shell, wood, coal, and other carbon sources that have low cost and are abundant in nature. Results obtained with these two pore models are directly compared here, as slit-shaped graphitic pores are often used as an approximate model for different activated carbon materials. We limit the scope of our paper to studying the structure and dynamics of ILs inside our model nanoporous materials in the absence of electrical charges in the pore walls, which is relevant not only to EDLCs but also to ionogels and IL-based nanomaterials (GUMBOS). The effect of applied electrical potentials and electrical charges in the pore walls on the properties of confined ILs will be considered later in a different manuscript. The rest of this paper is structured as follows. Section 2 contains a description of our computational models and methods. In section 3 we present results and a discussion of the structural and dynamic properties of the ILs confined in both model porous materials, and in section 4 we summarize our main findings.

2. COMPUTATIONAL DETAILS

All our classical molecular dynamics (MD) simulations involving ILs inside model porous carbons were performed using GROMACS 4.0.5 software⁸⁵ in the NVT ensemble. The IL [emim⁺][NTf₂⁻] (Figure 1) was modeled using parameters from Kelkar and Maginn.⁸⁶ This force field can adequately reproduce the experimental density, heat of vaporization, and diffusion coefficient of the bulk IL, as shown in ref 86 and corroborated by us in additional MD simulations of the bulk IL. Two pore models were considered in this study (Figure 2), a slit graphitic pore similar to the one used in our previous studies,^{53,55,56} and a realistic model of a CSAC developed by Pikunic et al.^{83,84} This model is very similar to the one developed by Thomson and Gubbins⁸⁷ and was generated using a reverse Monte Carlo simulation protocol in a way that the model material matches the experimental radial distribution

function $g(r)$ of a CSAC, subject to several physical constraints typical of graphitic carbons (namely that carbon atoms can only have two or three nearest neighbors, C–C distances are 1.42 Å, and bond angles are 120°). Additional details of the simulation protocol and the CSAC model material are presented in the original references.^{83,84,87} The CSAC model used here is composed of semigraphitic walls of different sizes and shapes and with a minor degree of corrugation, which form pores of roughly rectangular shape that are irregularly interconnected. As in our previous studies, the carbon atoms in our model porous materials were represented as Lennard–Jones spheres with $\epsilon_c/k = 28$ K and $\sigma_c = 0.340$ nm. All carbon materials were uncharged in this study.

We considered three pore sizes for our slit graphitic porous carbon, $H = 0.75$, 0.93, and 1.23 nm. These sizes were chosen based on the work of Wu et al.,⁴⁴ who reported a U-shaped curve for the capacitance of ILs inside slit-shaped pores, with the minimum in capacitance observed for a pore size of about 0.91 nm (however, those results were obtained for a coarse-grained model of a different IL, [dmim⁺][BF₄⁻]). The original CSAC model had a narrow pore size distribution that peaked at a pore size of about 0.4 nm,^{83,84} and contained about 30 000 carbon atoms in a simulation box with dimensions $X = Y = Z = 11.07$ nm. To reduce the computational cost of our calculations using this model material, we cut a section of size $x = 6.8$ nm, $y = 6.3$ nm and $z = 1.4$ nm from the original model material. This section is representative of the original model material and contains all its relevant physical features. To consider CSAC model materials with mean pore sizes $H = 0.75$, 0.93, and 1.23 nm, we took the section cut from the original model carbon and slightly increased the separation between the carbon layers in the z -direction while keeping the same x - and y -coordinates of each carbon atom, thus obtaining three different model materials with larger pore sizes. As a result of these operations, the x and y sizes of our CSAC model materials remained unaltered ($x = 6.8$ nm and $y = 6.3$ nm), but the z size changed according to the mean pore size (i.e., $z = 3.7$ nm for $H = 0.75$ nm; $z = 4.4$ nm for $H = 0.93$ nm; $z = 4.7$ nm for $H = 1.23$ nm). We then computed the pore size distribution (PSD) of each of these three model materials following the methodology described elsewhere^{87–89} and ensured that their PSDs peaked at the values $H = 0.75$, 0.93, and 1.23 nm. The PSDs are shown in Figure 3.

All our carbon model materials were placed in the center of an orthorhombic box, with periodic boundary conditions applied in all three directions. For the CSAC model, the y and z dimensions of the orthorhombic simulation box matched the y and z dimensions of the model carbon material (i.e., $L_y = 6.3$ nm, and $L_z = 3.7$, 4.4, and 4.7 nm for $H = 0.75$, 0.93, and 1.23 nm, respectively; see Table 1). The simulation box was elongated in the x -direction ($L_x = 20$ nm). For the slit graphitic pores, the total length of the box in the y -direction was equal to 5.8 nm, which was similar to the size in the y -direction of the carbon walls. The size of the carbon walls in the x -direction is 5.7 nm, and the total length of the simulation box in this direction was $L_x = 30$ nm. The total length of the box in the z -direction was 8 nm (Table 1), and therefore the slit pore was surrounded on top and bottom by two vacuum regions, which were large enough to avoid any interaction between the adsorbed ions and their nearest periodic image in the z -direction. These vacuum regions in the z -direction were not present in our simulations with the CSAC model (Table 1), and therefore the system involving the IL confined within the

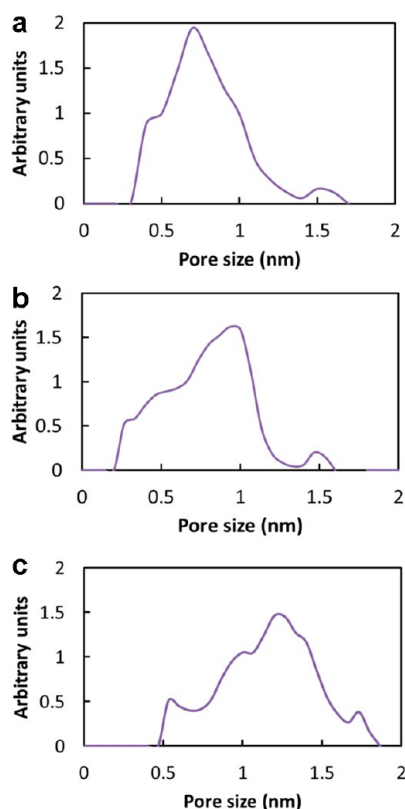


Figure 3. Pore size distributions (PSDs) of CSAC model considered in this work. The PSDs of the model materials peak at (a) $H = 0.75$ nm, (b) $H = 0.93$ nm, and (c) $H = 1.23$ nm.

Table 1. Systems Details

slit graphitic pore size H (nm)	number of IL pairs	dimensions of simulation box (x, y, z in nm)	amount of IL inside pore (ρ/ρ_{bulk}) ^a
0.75	192	$30.0 \times 5.8 \times 8.0$	1.22
0.93	288	$30.0 \times 5.8 \times 8.0$	1.04
1.23	288	$30.0 \times 5.8 \times 8.0$	1.14
coconut shell activated carbon model, average pore size (nm)	number of IL pairs	dimensions of simulation box (x, y, z in nm)	amount of IL inside pore (ρ/ρ_{bulk}) ^a
0.75	416	$20.0 \times 6.3 \times 3.7$	0.95
0.93	468	$20.0 \times 6.3 \times 4.4$	0.95
1.23	780	$20.0 \times 6.3 \times 4.7$	0.99

^aThe density ρ of IL inside the pores was calculated as $\rho = N/V$, where V is the pore volume. For the slit graphitic pore, $V = L_x L_y \times (H - \sigma_c)$, with $L_x = 5.7$ nm and L_y as given in the table above. For the CSAC model, $V = L_x L_y L_z - (\text{area of carbon sheets}) \times \sigma_c$, with $L_x = 6.8$ nm and L_y and L_z as given in the table above.

pores of the CSAC model was periodic in the y - and z -directions (Figure 2). In this work we considered a simulation setup in which our model porous carbons were directly connected to two reservoirs of IL at both sides (Figure 2). Initially, the ions are arranged in an arbitrary lattice outside of the pore, with auxiliary walls (made of model carbon atoms) closing the entrances to the pore. When the simulation starts, the auxiliary walls shown in Figure 2 are removed and the ions can enter (or exit) the porous material. Such a setup has been used in several previous studies of ILs inside nanopores^{44,50} and should yield a good estimation of the “equilibrium” amount of IL inside the nanopore. The amount of IL inside the carbon pores at the end of our simulations is reported in Table 1 as a percentage of the density of the bulk IL at the same temperature, together with additional details of our model systems. The bulk density in Table 1 refers to the simulated bulk density (~ 1.5 g/cm³) of the IL at 333 K, as obtained from separate MD simulations of this IL in the bulk. This value is about 3% larger than the reported experimental density of the same IL⁹⁰ but is comparable to the density obtained by Kelkar and Maginn.⁸⁶ We note here that the total numbers of IL pairs used in our simulations are indeed not enough to fill the large reservoir spaces located at both sides of the CSAC and slit pore models. As a result, two large vacuum regions will form at the left and right sides of the systems depicted at the bottom of Figure 2a (CSAC model) and 2b (slit pore model). We ran additional simulations with a larger number of ion pairs and found no significant differences in the properties of the IL confined inside the porous carbons (which are the focus of this study). The IL at the reservoirs at both sides of our model carbon pores (Figure 2) has a density similar to that of the bulk IL at the same temperature.

Our initial configurations were relaxed via energy minimizations using the steepest descent scheme. The IL in our systems were then melted at a temperature of 600 K and then annealed from 600 K to 333 K in six stages of 500 ps each. Once the system reached the desired temperature of 333 K, the auxiliary walls were removed and the ions were allowed to fill the pores during our MD simulation runs. The rest of our simulation details and methods are exactly the same as those described in our previous studies.^{53,55,56} In particular, all the dynamical properties reported in this paper were computed from our MD simulations in the NVT ensemble, where we used the improved velocity-rescaling thermostat of Parrinello et al.^{91,92} It has been shown that this algorithm can properly generate a canonical ensemble. In addition, Parrinello et al.^{91,92} computed the self-diffusivity of bulk TIP4P water at 300 K in NVT simulations with their thermostat and found that to be very similar to the values computed from NVE simulations and

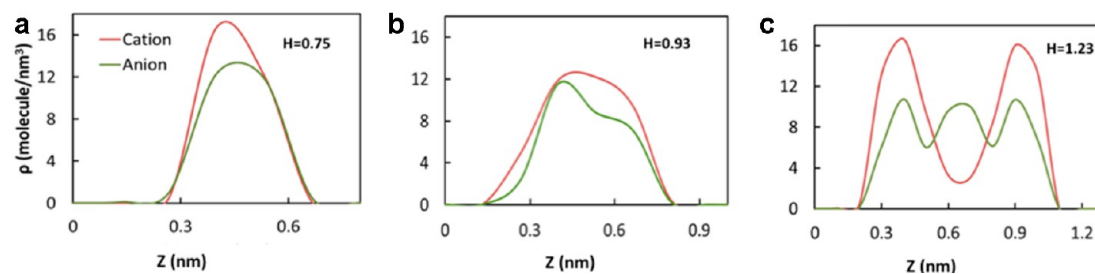


Figure 4. Number density profile of cations and anions vs z -coordinate, for the IL confined inside slit graphitic pores of widths (a) $H = 0.75$ nm, (b) $H = 0.93$ nm, and (c) $H = 1.23$ nm.

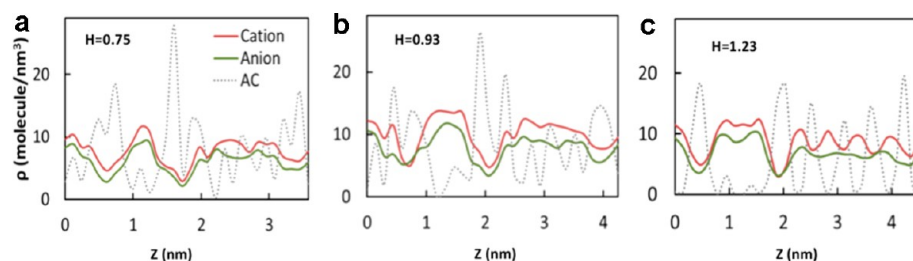


Figure 5. Number density profile of cations, anions, and carbons in the CSAC model systems with PSDs peaking at (a) $H = 0.75$ nm, (b) $H = 0.93$ nm, and (c) $H = 1.23$ nm. Densities were averaged over the x - y plane at any given value of the z -coordinate.

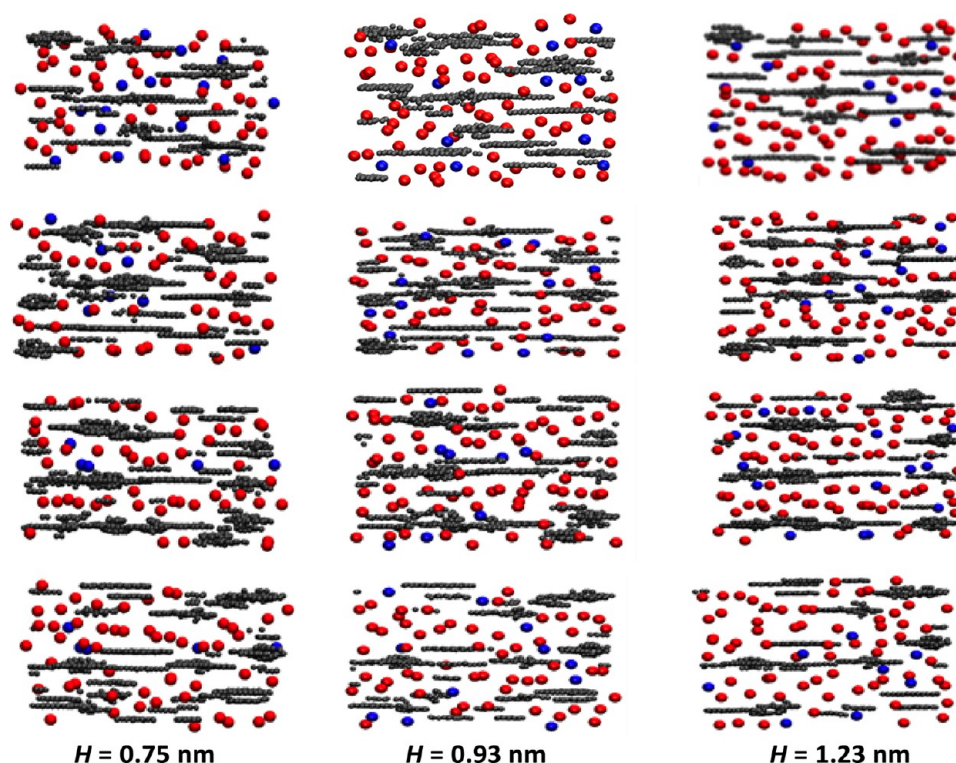


Figure 6. Cross sections (y - z plane at four different ranges of x) of representative simulation snapshots of the cations inside our coconut shell activated carbon models. Only the centers of mass of the cations are depicted. The cations are color-coded according to their orientation: blue and red spheres indicate $[\text{emim}^+]$ lying parallel or tilted with respect to the carbon surfaces. Four cross sections of our simulation boxes are shown: $5.5 \text{ nm} < x < 7.2 \text{ nm}$ (first row), $7.2 \text{ nm} < x < 8.9 \text{ nm}$ (second row), $8.9 \text{ nm} < x < 10.6 \text{ nm}$ (third row), and $10.3 \text{ nm} < x < 12.0 \text{ nm}$ (fourth row).

to those reported in the literature for the same model of water. They also computed the vibrational spectrum from the hydrogen atoms in ice I_h in NVT simulations with their thermostat and found it to be very similar to that determined from NVE simulations. These results suggest that this thermostat does not affect significantly the dynamical properties of the modeled systems.

3. RESULTS AND DISCUSSION

3.1. Structural Properties. We first examined the structure of cations and anions inside our CSAC models with three different PSDs peaking at $H = 0.75$, 0.93 , and 1.23 nm and compared those against results obtained for ILs inside slitlike graphitic pores with the same pore sizes H . These pore widths were chosen based on the work of Wu et al.,⁴⁴ who reported a U-shaped curve for the capacitance of ILs inside slit-shaped pores, with the minimum in capacitance observed for a pore size of about 0.91 nm. The capacitance depends on structural properties such as the density of ions inside the nanopores,

which is reported in Figures 4 and 5 for the slit pore and CSAC systems. However, here we only considered uncharged model porous electrodes. To establish a direct link between the density of the ions inside the nanopores and the capacitance, one would need to perform simulations considering both charged and uncharged porous electrodes. From the local density of the ions inside uncharged and charged electrodes, one could determine the electrical potential distribution inside the nanopores and then calculate the differential and effective capacitances which in turn can be related to experimental measurements (see, for example, refs 40, 44, 76, and references therein). For our simulations with uncharged CSAC and slit pore models, the density of ions (and of the carbon atoms in the pore walls of the coconut shell carbon) was averaged over the x - y plane (including only x values where the IL is inside the CSAC and slit pore models) at any given value of the z -coordinate, and the carbon walls do not have any electrical charges. The density profiles shown in Figure 4 for the ions inside slit graphitic nanopores show one layer of cations and anions when the pore size is $H = 0.75$ nm. As the pore size

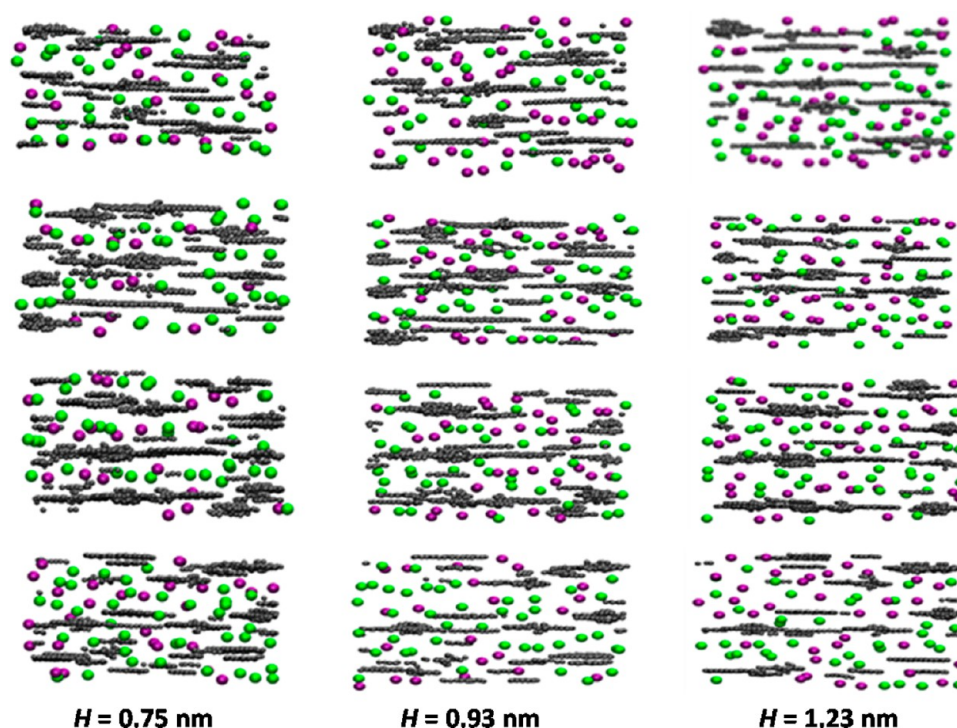


Figure 7. Cross sections (y – z plane at four different ranges of x) of representative simulation snapshots of the anions inside our coconut shell activated carbon models. Only the centers of mass of the anions are depicted. The anions are color-coded according to their orientation: green and purple spheres indicate $[\text{NTf}_2]^-$ lying parallel or tilted with respect to the carbon surfaces. Four cross sections of our simulation boxes are shown: $5.5 \text{ nm} < x < 7.2 \text{ nm}$ (first row), $7.2 \text{ nm} < x < 8.9 \text{ nm}$ (second row), $8.9 \text{ nm} < x < 10.6 \text{ nm}$ (third row), and $10.3 \text{ nm} < x < 12.0 \text{ nm}$ (fourth row).

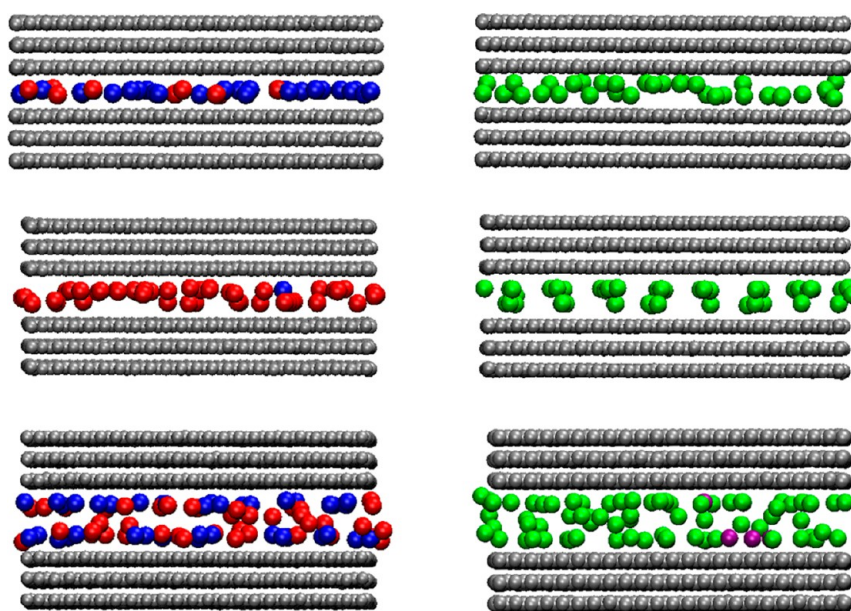


Figure 8. Side views of representative simulation snapshots of cations (left) and anions (right) inside slit graphitic pore models of widths $H = 0.75 \text{ nm}$ (top), 0.93 nm (center) and 1.23 nm (bottom). Only the centers of mass of the cations and anions are depicted, which are color-coded according to their orientation; for cations, blue and red spheres indicate $[\text{emim}]^+$ at $\theta < 25^\circ$ and $\theta > 25^\circ$ with respect to the carbon surfaces, and in the case of anions, green and purple beads indicate $[\text{NTf}_2]^-$ at $\theta < 25^\circ$ and $\theta > 25^\circ$ with respect to the pore walls.

increases to $H = 0.93 \text{ nm}$, the layer of cations and anions becomes wider to fill the accessible space. Increasing the pore size to $H = 1.23 \text{ nm}$ leads to the formation of two distinct layers of cations and three layers of anions (although these three layers are not as well-defined as the cations' layers, compare the magnitude of the minima in the density profiles of Figure 4). These results agree with those observed in previous studies⁴⁴

where the density profiles of ions, particularly in narrow uncharged pores such as the ones considered here, depend strongly on the pore size, geometry, and relative size of the ions. The equivalent density profiles for the CSAC model (Figure 5) are more complex due to the irregular nature of the model material (semigraphitic walls of different sizes and shapes forming irregularly connected pores of roughly

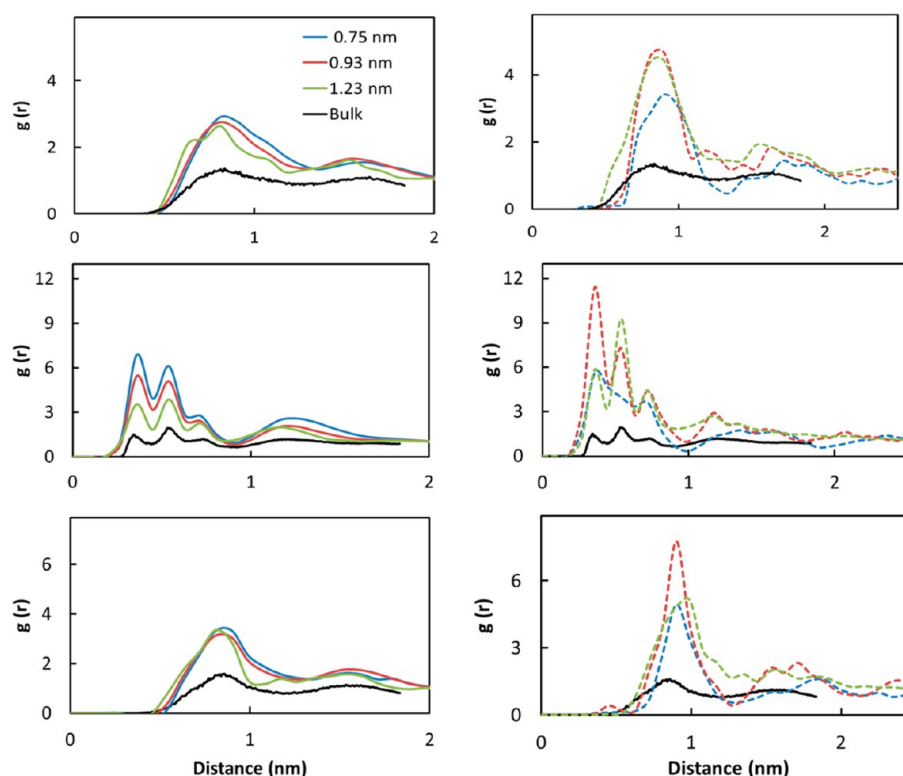


Figure 9. Cation–cation (top), cation–anion (center), and anion–anion (bottom) radial distribution functions $g(r)$ of the ions inside the CSAC model (left panel) and inside the slit graphitic pore model (right panel). $g(r)$ functions for the bulk IL are shown as black lines.

rectangular shape). As expected, in the CSAC model the ions fill the pore space where the density of carbon is low.

Further insights into the structure of the IL inside the CSAC model can be obtained from the cross sections (y – z plane at four different ranges of x) of representative simulation snapshots of the cations and anions inside our CSAC models, which are shown in Figures 6 and 7, respectively. Here we only depict the centers of mass of the cations (blue and red spheres, Figure 6) and anions (green and purple spheres, Figure 7), which are color-coded according to their orientation as measured by $\cos(\theta)$. Here, θ is the angle between a vector normal to the carbon surfaces, and the vector normal to the imidazolium ring (cations, Figure 1), or the vector joining the two carbon atoms (anions, Figure 1). In this analysis, we arbitrarily defined any ion that has $\theta < 25^\circ$ as lying parallel to the carbon surface, and all ions with $\theta > 25^\circ$ as tilted with respect to the surface. In Figure 6, blue spheres indicate $[\text{emim}^+]$ parallel to the carbon surfaces, and red spheres depict $[\text{emim}^+]$ with a tilted orientation with respect to the carbon walls. Similarly, in Figure 7 the anions are color coded with green spheres representing parallel orientations, and purple spheres depict tilted anions. The same snapshots showing the cations and anions together are presented in Figure S1 of the Supporting Information. The purpose of the representative snapshots shown in Figures 6 and 7 is to illustrate not only the orientation of the ions but also how they distribute inside the model CSAC material. We mainly show these figures because the pore geometry of the CSAC model material is very irregular (see also Figure 2), and thus the distribution of the ions as shown in these snapshots can complement the average density profiles reported in Figure 5. To complement the information about the orientation of the ions shown in Figures 6 and 7, we have also included plots of the average ion orientation along the

z -direction for the IL inside the CSAC model (Figure S2, Supporting Information). In Figure 6, the majority of the cations confined in the pores have a tilted orientation (red spheres); however, a significant fraction of the cations lie with a parallel orientation (blue spheres), especially when they are close to the carbon walls. In turn, in Figure 7 most of the anions adopt an orientation parallel to the carbon walls (green spheres), with a significant fraction lying tilted to the walls (purple spheres). These orientations contrast with those that were obtained for the ions inside the slit carbon model (Figure 8). For $H = 0.75$ nm, the cations and anions form a single layer inside the slit pore (Figure 4), with most of the cations and all of the anions lying parallel to the carbon walls. As the pore width increases to $H = 0.93$ nm, the layer of cations and anions becomes wider (Figure 4) and most of the cations adopt a tilted orientation ($\theta > 25^\circ$) whereas the anions still remain parallel to the carbon surfaces. As the pore size increases to $H = 1.23$ nm, we observe formation of two layers of cations (Figure 4), with some of the cations lying parallel and some tilted to the carbon surfaces (Figure 8); this increase in pore size allows a few of the anions to adopt a tilted orientation. Although the coconut shell and the graphitic slit pore carbon models have similar pore sizes, the differences in orientation of the ions inside the two pore models are caused by the intrinsic properties of the CSAC model, namely the presence of (1) a distribution of pore sizes and (2) irregularly connected pores formed by the carbon sheets having different sizes and shapes (notice the marked differences in the configuration of the carbon walls and the pores between contiguous rows in Figures 6 and 7, and in Figure S1, Supporting Information). These structural heterogeneities in the CSAC model also cause the ions to exhibit more irregular variations in their densities (Figures 5–7; see also Figure S1, Supporting Information), as opposed to the

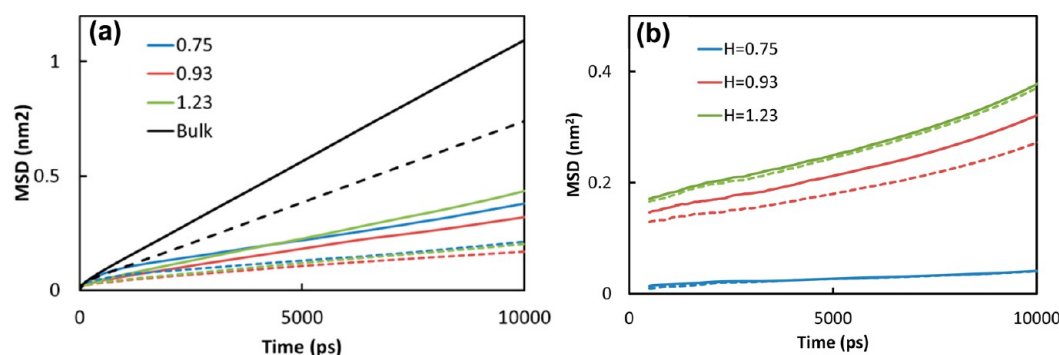


Figure 10. MSD in parallel direction (x and y) for [emim⁺] (solid lines) and [NTf₂[−]] (dashed lines) confined inside (a) CSAC model material, and (b) slit graphitic pore model, with three different pore sizes ($H = 0.75, 0.93$, and 1.23 nm).

well-defined layers of ions in the slit pore model (Figures 4 and 8). In the CSAC, some formation of layers of ions can still be observed in each particular y – z cross section (those are slightly more evident in Figures 6 and 7), but the irregularities in the size and shape of the carbon walls and in the pores cause those layers of ions to disappear as we move in the x -direction.

In Figure 9 we show the cation–cation, cation–anion, and anion–anion radial distribution functions $g(r)$ for the ions inside the CSAC and slit graphitic pore models. The CR carbon atom of [emim⁺] and the NJ nitrogen atom of [NTf₂[−]] (see Figure 1 for nomenclature) were chosen for this calculation, following previous studies.^{93,94} For the CSAC model material, we mainly observe differences in the heights of the peaks in the cation–anion $g(r)$ as the pore size decreases. Similar trends are observed for the cation–cation and anion–anion $g(r)$, although those functions for $H = 1.23$ nm exhibit minor differences in the positions of their peaks with respect to those observed in the two other pore sizes studied, $H = 0.75$ nm and $H = 0.93$ nm. In general, variations in the pore size of the CSAC model materials do not lead to significant variations in the position of the peaks in the $g(r)$ functions, which in turn are very similar to those observed for the bulk IL. These results suggest that the liquid structure of the IL confined inside the CSAC model materials is very similar to that of the bulk IL. Variations in the pore size in the slit graphitic pore model lead to more noticeable differences in the $g(r)$ functions, mainly in the height of the peaks but also in their positions. In particular, the second peak in the cation–anion $g(r)$ (at a distance $r \sim 0.5$ nm) disappeared when the IL is confined inside the narrowest slit pore considered here, $H = 0.75$ nm. This issue was not observed when the IL is inside the CSAC model with the same pore size, mainly because of its distribution of pore sizes (Figure 3) where pores much larger than 0.75 nm are present in this model material. The peaks observed in the cation–anion $g(r)$ at distances $r < 1.0$ nm are all related to the number of NJ atoms of the anion in the nearest-neighbor shell of the CR atom of the cations and vice versa; therefore, these peaks are also related to the formation of hydrogen bonds between the cations and anions.^{93,94} The fact that the second peak of the cation–anion $g(r)$ disappeared when the IL is inside the slit pore of $H = 0.75$ nm suggests that extremely large confinement effects can lead to significant changes in the liquid structure of the IL. This observation also suggests that the IL inside a slit pore of $H = 0.75$ nm experiences significantly larger confinement effects as compared to when the IL is inside the CSAC model with the same nominal pore size. The significant changes observed in the $g(r)$ of the IL confined inside the

narrow slit carbon pores considered here ($H = 0.75, 0.93$, and 1.23 nm) contrast with the results described in our previous study⁵⁵ for the same IL inside larger slit carbon pores ($H = 1.9, 2.5$, and 5.2 nm), where the different layers of ions (of width as low as 0.5 nm) had a liquid structure that was similar to that of the bulk IL.

The IL inside the slit pore model has a quasi-2D behavior. From Figure 4, only one layer of IL of width ~ 0.3 nm is present in the system with $H = 0.75$ nm. This layer becomes wider (~ 0.6 nm) for $H = 0.93$, and different layers are observed for $H = 1.23$ nm. Therefore, the ions have limited (but nonzero) motion along the z -direction; narrower slit pores ($H < 0.75$ nm) would be needed for the confined IL to exhibit a behavior that is rigorously two-dimensional. The radial distribution functions reported in the right panel of Figure 9 for the IL inside these slit pore models accurately reflect the fact that these systems have a behavior that is quasi-2D, as these radial distribution functions are significantly different from those of a (3D) bulk IL at the same temperature. In contrast, the IL inside the CSAC model materials has more freedom to move in the z -direction, because of the fact that the carbon sheets have irregular shape (e.g., see Figures 6 and 7), and therefore the radial distribution functions of the confined IL (left panel of Figure 9) are similar to that of the bulk IL at the same temperature.

3.2. Dynamical Properties. In Figure 10 we show the parallel component (x - and y -directions) of the mean squared displacement (MSD) of the cations and anions confined inside the CSAC model (Figure 10a) and within a slit graphitic pore (Figure 10b) with three different pore sizes. We did not report the z -component of the MSD of the confined ILs in this study. In our previous studies of ILs inside slit pore models,^{53,55,56,73} where the ions form layers of fluid parallel to the pore walls, we reported the MSDs in the x -, y - and z -direction, as well as determined how the MSDs varies for the different layers of IL. In those studies we showed that the z -component of the MSD is significantly smaller than the x - and y -components, and that the layers of ions close to the pore walls have dynamics that are significantly slower than those of the layers of ions in the center of the pore. We did not attempt to perform such an analysis in this work for brevity. In analogy to what we observed in our previous studies,^{53,55,56} the cations move faster than the anions, and the ions in bulk systems move significantly faster than those inside the pores of the CSAC model material or the slit graphitic pore. For the IL inside the CSAC model (Figure 10a), the fastest dynamics are observed inside the material of mean pore size $H = 1.23$ nm, followed by those inside of the material

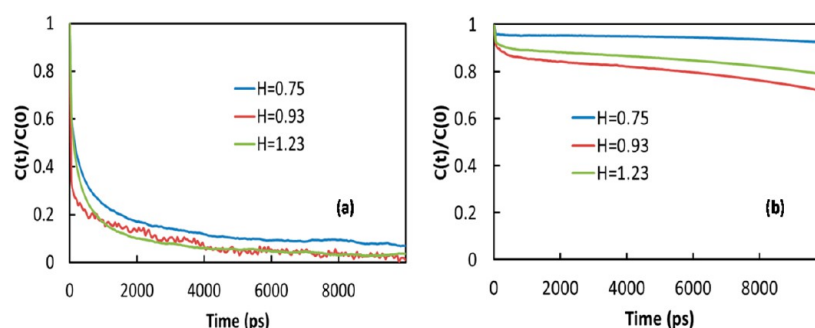


Figure 11. Single-particle time correlation function for the reorientation of cations inside the (a) CSAC model and (b) slit graphitic pore model. The correlation function shown represents the reorientation of cations around an axis perpendicular to their imidazolium ring.

with the $H = 0.75$ nm system; the ILs exhibit the slowest dynamics in the $H = 0.93$ nm model material. When H is reduced from 0.93 to 0.75 nm, the dynamics of the cations and anions increase 32% and 23%, respectively; likewise, as we increase H from 0.93 to 1.26 nm, the MSD of the cations and anions increase 70% and 15%, respectively. However, we note that the absolute difference in the MSD of the ions inside our three CSAC model materials is very small (less than 0.1 nm^2 at $t = 10 \text{ ns}$). The dynamics of the cations and anions inside slit graphitic nanopores (Figure 10b) increase monotonically with an increase in pore size from 0.75 to 1.23 nm, in agreement with what we observed in our previous study of the same IL inside slit graphitic pores with larger sizes.⁵⁵ This non-monotonous variation in the dynamics of the IL inside the CSAC material with increases in pore size was also observed in our previous study of an IL inside multiwalled carbon nanotubes, at some of the values of pore loading (ρ/ρ_{bulk}) that we studied.⁶⁶ We also observed nonmonotonous variations in the MSD of the confined ions as we varied the amount of IL inside carbon pores of different shapes;^{53,55,66,79} in those studies, we discussed that varying the amount of IL inside the carbon pores induces the formation of regions with high and low density of IL, which in turn causes complex changes in the dynamics of the confined ions. We note that we observed slight variations in the density of the IL inside the CSAC model materials with different average pore sizes (Table 1). Furthermore, the PSDs of the model CSAC materials with $H = 0.75$ nm and $H = 0.93$ nm (Figure 3) are very similar, i.e., the minimum and maximum pore sizes are the same in both materials, and only the average pore size is different. Those factors, combined with the fact that the irregular pore geometry and the spatial variation in pore size within the CSAC model materials (which are discussed in detail in Figures 12–14 below) could explain the nonmonotonic (but small) variation of the dynamics of the IL with average pore size in our CSAC model materials (Figure 10a). Returning to the slit pore system, surprisingly the anions inside the slit pores (Figure 10b) show mobility similar to that of the cations inside the slit pores of width $H = 0.75$ and 1.23 nm. These surprising observations could be caused by the fact that these are very narrow pores, which only allow the formation of one to two layers of cations and one to three layers of anions; the high degree of confinement could slow down the dynamics to the point where anions can have mobilities similar to those of cations in some of these systems. The dynamics of the ILs inside the slit graphitic pores are much slower than those observed for the bulk IL, mainly because very narrow pores were considered in this work; in our previous study where larger slit pores were

considered,⁵⁵ the dynamics of the IL inside a slit graphitic pore of $H = 5.2$ nm were similar to those of the bulk IL.

Comparing the dynamics observed for the IL inside both pore models, we observe that in general the ions have faster dynamics inside the CSAC model than inside a slit graphitic pore of the same size. This observation is further illustrated in Figure 11, where we present the single-particle time correlation function of the reorientation of the cations around an axis perpendicular to their imidazolium ring cations, when they are confined inside both carbon models of different pore sizes. These results indicate that the rotational motion of the cations decorrelates (i.e., the correlation function reaches values close to zero) when the cations are inside the CSAC model. In contrast, the rotational motion of cations inside the slit pore model still shows significant correlation effects after 10 ns of simulation time. These observations are caused by the distribution of pore sizes and the irregularly connected pores formed by carbon sheets of different sizes and shapes in the CSAC model. These properties result in nonuniform confinement effects that are in general smaller than those observed in a slit graphitic pore model of the same nominal size, where confinement effects are much larger and lead to a significant reduction in the mobility of the ions. It is interesting to note that the MSDs of the cations inside the slit pore (Figure 10b) decrease monotonically as the pore size H decreases; on the other hand, the reorientation of the cations (Figure 11b) decorrelates faster for $H = 0.93$ nm, followed by $H = 1.23$ nm and $H = 0.75$ nm. This behavior can be related to the differences in the density profiles observed for $H = 0.93$ nm and $H = 1.23$ nm (Figures 4 and 8; one thick layer of cations and anions are observed for $H = 0.93$ nm, whereas for $H = 1.23$ nm there are two layers of cations and three layers of anions), which might cause the translational and rotational motion of the cations to follow slightly different trends. Nevertheless, the translational and rotational motions of the cations do not necessarily have to follow the same trends; for example, Hu and Margulis⁹⁵ showed that for bulk $[\text{bmim}^+][\text{PF}_6^-]$, the translational and rotational motion are decoupled for the anion and coupled for the cation.

Results from our previous studies^{53,55,56,66,73,79} suggest that the dynamics (as well as the structure) of confined ILs are a result of a complex interplay between different factors: (1) chemical nature of the pore walls, which affect the interactions with the IL ions (e.g., ILs have different properties when confined inside porous carbon, silica, or titania materials); (2) density of IL inside the nanopores, which in some cases can induce the formation of highly inhomogeneous phases; (3) distance of the ions to the pore walls; (4) pore size, pore shape

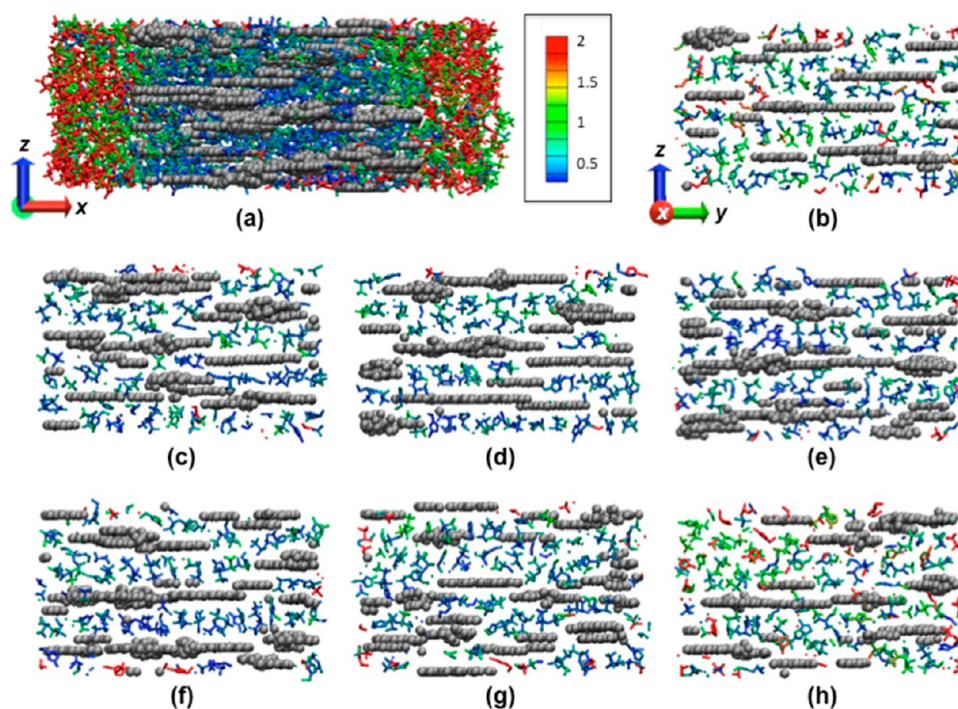


Figure 12. Representative simulation snapshots of [emim⁺][NTf₂⁻] inside a CSAC model with $H = 0.75$ nm. Cations and anions are color-coded according to their total displacement (in nm) over a time of 10 ns. (a) Snapshot (x - z view) of the whole system. (b-h) Cross section views of the cations and anions inside the CSAC model material; the figures depict y - z views of seven "slices" of the system (slice thickness $\Delta x = 1$ nm) at increasing values of the x -coordinate, where the slices shown in b and h are close to the bulklike reservoirs of IL (left and right sides of a).

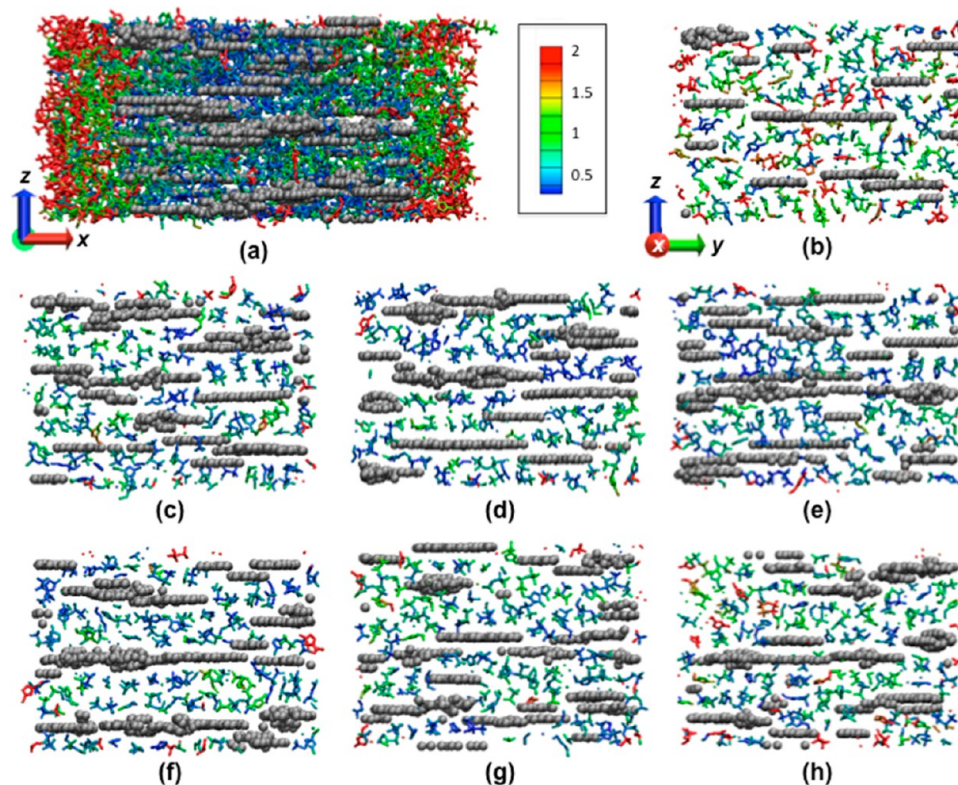


Figure 13. Representative simulation snapshots of [emim⁺][NTf₂⁻] inside a CSAC model with $H = 0.93$ nm. Cations and anions are color-coded according to their total displacement (in nm) over a time of 10 ns. (a) Snapshot (x - z view) of the whole system. (b-h) Cross section views of the cations and anions inside the CSAC model material; the figures depict y - z views of seven "slices" of the system (slice thickness $\Delta x = 1$ nm) at increasing values of the x -coordinate, where the slices shown in b and h are close to the bulklike reservoirs of IL (left and right sides of a).

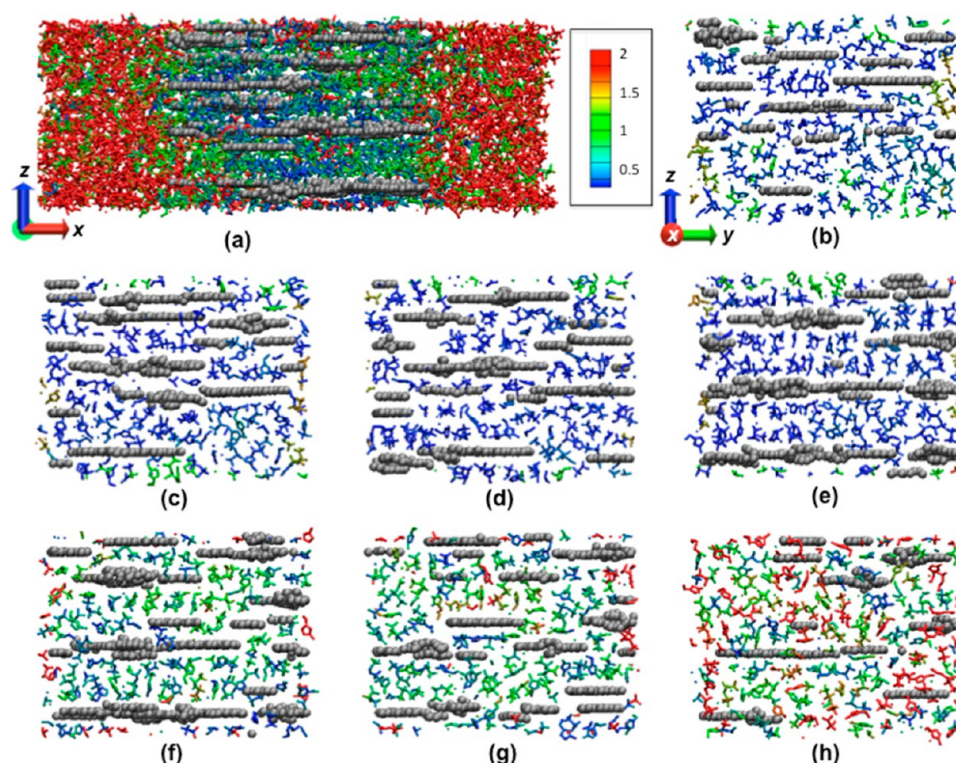


Figure 14. Representative simulation snapshots of $[\text{emim}^+][\text{NTf}_2^-]$ inside a CSAC model with $H = 1.23$ nm. Cations and anions are color-coded according to their total displacement (in nm) over a time of 10 ns. (a) Snapshot (x - z view) of the whole system. (b–h) Cross section views of the cations and anions inside the CSAC model material; the figures depict y - z views of seven “slices” of the system (slice thickness $\Delta x = 1$ nm) at increasing values of the x -coordinate, where the slices shown in b and h are close to the bulklike reservoirs of IL (left and right sides of a).

and surface roughness; (5) surface density of electrical charges in the pore walls. These factors, when combined with the heterogeneities in pore size, pore shape and surface roughness present in real porous materials, can cause the dynamics of the confined ILs to vary nonmonotonically with pore size (Figure 10a). To discuss further the dynamics of ILs inside our CSAC models, we show representative simulation snapshot of the whole system, as well as cross section views (y - z plane at seven different ranges of x) of the cations and anions inside our CSAC models with $H = 0.75$ nm (Figure 12), $H = 0.93$ nm (Figure 13), and $H = 1.23$ nm (Figure 14). In these figures we have color-coded the ions according to their total displacement during a time of 10 ns. The results shown in Figures 12–14 suggest that the ions inside the CSAC model materials also exhibit heterogeneous dynamics, in analogy to what we observed for ILs inside regular slit graphitic nanopores.^{53,55} In general, we observe that the ions in the reservoirs at both sides of the CSAC model materials move faster than the ions inside the pores (Figures 12a, 13a, and 14a). The ions inside the pores but close to the reservoirs (Figures 12b,h, 13b,h, and 14b,h) have faster dynamics than those ions that are deeper inside the CSAC model materials. In analogy to what we observed for ILs inside regular slit pores made of graphite^{53,55} or titania,⁷³ the results shown in Figures 12–14 also suggest that both cations and anions become slower in the regions near the pore walls, exhibiting slightly faster dynamics when they are farther away from the carbon walls. However, the complex pore geometry and the variation of pore size with position within the CSAC model material cause the structure and the dynamics of the confined IL to depart significantly from the more uniform behavior observed in slit nanopores. Important spatial variations and heterogeneities in the dynamics are observed

for all systems. For example, for the CSAC with $H = 1.23$ nm, most of the ions are colored blue in the snapshots shown in Figure 14c–e, but they have increased mobilities in the snapshots shown in Figure 14f,g. This behavior might be linked to the irregular pore morphology, as the ions exhibit faster dynamics when they are in open spaces within the porous network (i.e., in the nanometer-sized regions where pore size is slightly larger); the ions have and slower dynamics in the regions where the carbon walls are closer to each other and the pore sizes are smaller. Spatial variations in pore size and shape, as well as irregular pore geometry, might also be linked to the nonmonotonic (but small) variation in the dynamics of the confined IL with average pore size of the CSAC material (Figure 10a).

4. CONCLUSIONS

Classical molecular dynamics simulations were performed to study the structure and dynamics of the ionic liquid (IL) $[\text{emim}^+][\text{NTf}_2^-]$ inside two model porous carbon materials, a slit graphitic nanopore and a realistic model of a coconut shell activated carbon (CSAC). This last model material was generated using a reverse Monte Carlo protocol and matches the experimental radial distribution from samples of the real adsorbent. The CSAC model material consists of semigraphitic carbon sheets with different sizes and shapes, which form irregularly connected pores of roughly rectangular shape. Three average pore sizes were considered for both types of model materials, $H = 0.75$, 0.93 , and 1.23 nm. In general, the ions inside the CSAC model material form layers parallel to the walls, in analogy to the arrangement observed inside slit pores; however, the distribution of pore sizes and the complex pore

geometry of the CSAC model materials cause the density profiles and the orientation of the ions to depart significantly from the uniform behavior observed for these properties inside slit pores. Furthermore, the presence of interconnected pores with a distribution of sizes in the CSAC model materials cause confinement effects to be weaker than those observed in slit nanopores of the same average size. For example, the liquid structure of the ions inside CSAC model materials is very similar to that of the bulk IL; in contrast, marked differences with respect to the $g(r)$ of the bulk IL were observed for the ions inside the narrow slit pores considered in this study. The dynamics of the IL inside the CSAC model materials were significantly faster than those observed inside slit pores of the same average size. The dynamics of ions become monotonically faster as the size of the slit pore increases, but an increase in average pore size in the CSAC model materials lead to a nonmonotonic (but small) variation in the dynamics of the confined ions. In analogy to what was observed in slit pores, the ions near the pore walls of the CSAC model material also move slower than the ions that are farther away from the walls; however, the complex pore geometry of the CSAC model material cause the dynamics of the confined IL to exhibit significant spatial heterogeneities and to depart significantly from the uniform, regular behavior observed in slit nanopores (where the ions arrange in layers, and those layers closer to the pore walls move slower than the layers of ions that are in the center of the pore and farther from the walls). Our results suggest that the structure and dynamics of ILs confined inside porous materials having heterogeneities in pore size, pore shape, and pore interconnectivity can depart significantly from the properties of ILs confined inside ideal pores of simple geometries.

The scope of this paper was limited to studying the structure and dynamics of ILs inside our model nanoporous materials in the absence of electrical charges in the pore walls, which is relevant not only to EDLCs but also to ionogels and IL-based nanomaterials (GUMBOS). The effect of applied electrical potentials and electrical charges in the pore walls on the properties of confined ILs will be considered later in a different manuscript.

■ ASSOCIATED CONTENT

■ Supporting Information

Figures S1 (cross sections of representative simulation snapshots of the center of mass of cations and anions, color-coded according to their orientation, inside our CSAC models) and S2 (orientation of cations and anions, and number density profiles of carbon atoms in our CSAC models). This material is available free of charge via the Internet at <http://pubs.acs.org>.

■ AUTHOR INFORMATION

Corresponding Author

*E-mail: frhung@lsu.edu.

Author Contributions

[†]These authors contributed equally to the work.

Notes

The authors declare no competing financial interest.

■ ACKNOWLEDGMENTS

We are grateful to Jeremy Palmer (Princeton) for his help in determining the pore size distribution of the carbon models used in this study. This work was partially supported by the

National Science Foundation (CAREER Award CBET-1253075, and EPSCoR Cooperative Agreement EPS-1003897) and by the Louisiana Board of Regents. High-performance computational resources for this research were provided by High Performance Computing at Louisiana State University (<http://www.hpc.lsu.edu>) and the Louisiana Optical Network Initiative (<http://www.loni.org>).

■ REFERENCES

- (1) Conway, B. E. *Electrochemical Supercapacitors: Scientific Fundamentals and Technological Applications*; Kluwer Academic/Plenum Publishers: New York, 1999.
- (2) Zhang, L. L.; Zhao, X. S. Carbon-Based Materials as Supercapacitor Electrodes. *Chem. Soc. Rev.* **2009**, *38*, 2520–2531.
- (3) Simon, P.; Gogotsi, Y. Materials for Electrochemical Capacitors. *Nat. Mater.* **2008**, *7*, 845–854.
- (4) Frackowiak, E. Carbon Materials for Supercapacitor Application. *Phys. Chem. Chem. Phys.* **2007**, *9*, 1774–1785.
- (5) Pandolfo, A. G.; Hollenkamp, A. F. Carbon Properties and Their Role in Supercapacitors. *J. Power Sources* **2006**, *157*, 11–27.
- (6) Presser, V.; Heon, M.; Gogotsi, Y. Carbide-Derived Carbons - From Porous Networks to Nanotubes and Graphene. *Adv. Funct. Mater.* **2011**, *21*, 810–833.
- (7) Zhai, Y. P.; Dou, Y. Q.; Zhao, D. Y.; Fulvio, P. F.; Mayes, R. T.; Dai, S. Carbon Materials for Chemical Capacitive Energy Storage. *Adv. Mater.* **2011**, *23*, 4828–4850.
- (8) Choi, N. S.; Chen, Z. H.; Freunberger, S. A.; Ji, X. L.; Sun, Y. K.; Amine, K.; Yushin, G.; Nazar, L. F.; Cho, J.; Bruce, P. G. Challenges Facing Lithium Batteries and Electrical Double-Layer Capacitors. *Angew. Chem., Int. Ed.* **2012**, *51*, 9994–10024.
- (9) Armand, M.; Endres, F.; MacFarlane, D. R.; Ohno, H.; Scrosati, B. Ionic-Liquid Materials for the Electrochemical Challenges of the Future. *Nat. Mater.* **2009**, *8*, 621–629.
- (10) Arbizzani, C.; Biso, M.; Cericola, D.; Lazzari, M.; Soavi, F.; Mastragostino, M. Safe, High-Energy Supercapacitors Based on Solvent-Free Ionic Liquid Electrolytes. *J. Power Sources* **2008**, *185*, 1575–1579.
- (11) Mastragostino, M.; Soavi, F. Strategies for High-Performance Supercapacitors for HEV. *J. Power Sources* **2007**, *174*, 89–93.
- (12) Balducci, A.; Dugas, R.; Taberna, P. L.; Simon, P.; Plee, D.; Mastragostino, M.; Passerini, S. High Temperature Carbon-Carbon Supercapacitor Using Ionic Liquid as Electrolyte. *J. Power Sources* **2007**, *165*, 922–927.
- (13) Lazzari, M.; Soavi, F.; Mastragostino, M. High Voltage, Asymmetric EDLCs Based on Xerogel Carbon and Hydrophobic IL Electrolytes. *J. Power Sources* **2008**, *178*, 490–496.
- (14) Galinski, M.; Lewandowski, A.; Stepniak, I. Ionic Liquids as Electrolytes. *Electrochim. Acta* **2006**, *51*, 5567–5580.
- (15) Lu, W.; Qu, L. T.; Henry, K.; Dai, L. M. High Performance Electrochemical Capacitors from Aligned Carbon Nanotube Electrodes and Ionic Liquid Electrolytes. *J. Power Sources* **2009**, *189*, 1270–1277.
- (16) Barisci, J. N.; Wallace, G. G.; MacFarlane, D. R.; Baughman, R. H. Investigation of Ionic Liquids as Electrolytes for Carbon Nanotube Electrodes. *Electrochem. Commun.* **2004**, *6*, 22–27.
- (17) Largeot, C.; Portet, C.; Chmiola, J.; Taberna, P. L.; Gogotsi, Y.; Simon, P. Relation between the Ion Size and Pore Size for an Electric Double-Layer Capacitor. *J. Am. Chem. Soc.* **2008**, *130*, 2730–2731.
- (18) Lin, R.; Huang, P.; Segalini, J.; Largeot, C.; Taberna, P. L.; Chmiola, J.; Gogotsi, Y.; Simon, P. Solvent Effect on the Ion Adsorption from Ionic Liquid Electrolyte into Sub-Nanometer Carbon Pores. *Electrochim. Acta* **2009**, *54*, 7025–7032.
- (19) Le Bideau, J.; Viau, L.; Vioux, A. Ionogels, Ionic Liquid Based Hybrid Materials. *Chem. Soc. Rev.* **2011**, *40*, 907–925.
- (20) Vioux, A.; Viau, L.; Volland, S.; Le Bideau, J. Use of Ionic Liquids in Sol-Gel; Ionogels and Applications. *C. R. Chim.* **2010**, *13*, 242–255.

- (21) Lunstroot, K.; Driesen, K.; Nockemann, P.; Van Hecke, K.; Van Meervelt, L.; Gorller-Walrand, C.; Binnemans, K.; Bellayer, S.; Viau, L.; Le Bideau, J.; Vioux, A. Lanthanide-Doped Luminescent Ionogels. *Dalton Trans.* **2009**, 298–306.
- (22) Lunstroot, K.; Driesen, K.; Nockemann, P.; Gorller-Walrand, C.; Binnemans, K.; Bellayer, S.; Le Bideau, J.; Vioux, A. Luminescent Ionogels Based on Europium-Doped Ionic Liquids Confined within Silica-Derived Networks. *Chem. Mater.* **2006**, *18*, 5711–5715.
- (23) Néouze, M.-A.; Bideau, J. L.; Gaveau, P.; Bellayer, S. v.; Vioux, A. Ionogels, New Materials Arising from the Confinement of Ionic Liquids within Silica-Derived Networks. *Chem. Mater.* **2006**, *18*, 3931–3936.
- (24) Tesfai, A. E.-Z. B.; Bwambok, D. K.; Baker, G. A.; Fakayode, S. O.; Lowry, M.; Warner, I. M. Controllable Formation of Ionic Liquid Micro- and Nanoparticles via a Melt-Emulsion-Quench Approach. *Nano Lett.* **2008**, *8*, 897–901.
- (25) Tesfai, A.; El-Zahab, B.; Kelley, A. T.; Li, M.; Garino, J. C.; Baker, G. A.; Warner, I. M. Magnetic and Nonmagnetic Nanoparticles from a Group of Uniform Materials Based on Organic Salts. *ACS Nano* **2009**, *3*, 3244–3250.
- (26) Bwambok, D. K.; El-Zahab, B.; Challa, S. K.; Li, M.; Chandler, L.; Baker, G. A.; Warner, I. M. Near-Infrared Fluorescent Nano-GUMBOS for Biomedical Imaging. *ACS Nano* **2009**, *3*, 3854–3860.
- (27) Das, S.; Bwambok, D.; El-Zahab, B.; Monk, J.; de Rooy, S. L.; Challa, S.; Li, M.; Hung, F. R.; Baker, G. A.; Warner, I. M. Nontemplated Approach to Tuning the Spectral Properties of Cyanine-Based Fluorescent NanoGUMBOS. *Langmuir* **2010**, *26*, 12867–12876.
- (28) Dumke, J. C.; El-Zahab, B.; Challa, S.; Das, S.; Chandler, L.; Tolocka, M.; Hayes, D. J.; Warner, I. M. Lanthanide-Based Luminescent NanoGUMBOS. *Langmuir* **2010**, *26*, 15599–15603.
- (29) de Rooy, S. L.; El-Zahab, B.; Li, M.; Das, S.; Broering, E.; Chandler, L.; Warner, I. M. Fluorescent One-Dimensional Nanostructures from a Group of Uniform Materials Based on Organic Salts. *Chem. Commun.* **2011**, 47, 8916–8918.
- (30) Regmi, B. P.; Monk, J.; El-Zahab, B.; Das, S.; Hung, F. R.; Hayes, D. J.; Warner, I. M.; Novel, A. Composite Film for Detection and Molecular Weight Determination of Organic Vapors. *J. Mater. Chem.* **2012**, *22*, 13732–13741.
- (31) *Ionic Liquids in Synthesis*, 2nd ed.; Wasserscheid, P.; Welton, T., Eds.; Wiley-VCH: Weinheim, 2008.
- (32) Plechkova, N. V.; Seddon, K. R. Applications of Ionic Liquids in the Chemical Industry. *Chem. Soc. Rev.* **2008**, *37*, 123–150.
- (33) Lynden-Bell, R. M.; Del Popolo, M. G.; Youngs, T. G. A.; Kohanoff, J.; Hanke, C. G.; Harper, J. B.; Pinilla, C. C. Simulations of Ionic Liquids, Solutions, and Surfaces. *Acc. Chem. Res.* **2007**, *40*, 1138–1145.
- (34) Pinilla, C.; Del Popolo, M. G.; Kohanoff, J.; Lynden-Bell, R. M. Polarization Relaxation in an Ionic Liquid Confined between Electrified Walls. *J. Phys. Chem. B* **2007**, *111*, 4877–4884.
- (35) Pinilla, C.; Del Popolo, M. G.; Lynden-Bell, R. M.; Kohanoff, J. Structure and Dynamics of a Confined Ionic Liquid. Topics of Relevance to Dye-Sensitized Solar Cells. *J. Phys. Chem. B* **2005**, *109*, 17922–17927.
- (36) Reed, S. K.; Madden, P. A.; Papadopoulos, A. Electrochemical Charge Transfer at a Metallic Electrode: A Simulation Study. *J. Chem. Phys.* **2008**, *128*, 124701.
- (37) Sha, M. L.; Wu, G. Z.; Fang, H. P.; Zhu, G. L.; Liu, Y. S. Liquid-to-Solid Phase Transition of a 1,3-Dimethylimidazolium Chloride Ionic Liquid Monolayer Confined between Graphite Walls. *J. Phys. Chem. C* **2008**, *112*, 18584–18587.
- (38) Sha, M. L.; Wu, G. Z.; Liu, Y. S.; Tang, Z. F.; Fang, H. P. Drastic Phase Transition in Ionic Liquid [Dmim][Cl] Confined between Graphite Walls: New Phase Formation. *J. Phys. Chem. C* **2009**, *113*, 4618–4622.
- (39) Merlet, C.; Salanne, M.; Rotenberg, B.; Madden, P. A. Imidazolium Ionic Liquid Interfaces with Vapor and Graphite: Interfacial Tension and Capacitance from Coarse-Grained Molecular Simulations. *J. Phys. Chem. C* **2011**, *115*, 16613–16618.
- (40) Feng, G.; Zhang, J. S.; Qiao, R. Microstructure and Capacitance of the Electrical Double Layers at the Interface of Ionic Liquids and Planar Electrodes. *J. Phys. Chem. C* **2009**, *113*, 4549–4559.
- (41) Tazi, S.; Salanne, M.; Simon, C.; Tury, P.; Pounds, M.; Madden, P. A. Potential-Induced Ordering Transition of the Adsorbed Layer at the Ionic Liquid/Electrified Metal Interface. *J. Phys. Chem. B* **2010**, *114*, 8453–8459.
- (42) Fedorov, M. V.; Kornyshev, A. A. Ionic Liquid near a Charged Wall: Structure and Capacitance of Electrical Double Layer. *J. Phys. Chem. B* **2008**, *112*, 11868–11872.
- (43) Reed, S. K.; Lanning, O. J.; Madden, P. A. Electrochemical Interface between an Ionic Liquid and a Model Metallic Electrode. *J. Chem. Phys.* **2007**, *126*, 084704.
- (44) Wu, P.; Huang, J.; Meunier, V.; Sumpter, B. G.; Qiao, R. Complex Capacitance Scaling in Ionic Liquids-Filled Nanopores. *ACS Nano* **2011**, *5*, 9044–9051.
- (45) Feng, G.; Cummings, P. T. Supercapacitor Capacitance Exhibits Oscillatory Behavior as a Function of Nanopore Size. *J. Phys. Chem. Lett.* **2011**, 2859–2864.
- (46) Jiang, D.-e.; Jin, Z.; Wu, J. Oscillation of Capacitance inside Nanopores. *Nano Lett.* **2011**, *11*, 5373–5377.
- (47) Kondrat, S.; Kornyshev, A. Superionic State in Double-Layer Capacitors with Nanoporous Electrodes. *J. Phys.: Condens. Matter* **2011**, *23*, 022201.
- (48) Kondrat, S.; Georgi, N.; Fedorov, M. V.; Kornyshev, A. A.; Superionic, A. State in Nano-Porous Double-Layer Capacitors: Insights from Monte Carlo Simulations. *Phys. Chem. Chem. Phys.* **2011**, *13*, 11359–11366.
- (49) Feng, G.; Huang, J. S.; Sumpter, B. G.; Meunier, V.; Qiao, R. A “Counter-Charge Layer in Generalized Solvents” Framework for Electrical Double Layers in Neat and Hybrid Ionic Liquid Electrolytes. *Phys. Chem. Chem. Phys.* **2011**, *13*, 14723–14734.
- (50) Feng, G. A.; Qiao, R.; Huang, J. S.; Sumpter, B. G.; Meunier, V. Atomistic Insight on the Charging Energetics in Subnanometer Pore Supercapacitors. *J. Phys. Chem. C* **2010**, *114*, 18012–18016.
- (51) Feng, G.; Qiao, R.; Huang, J. S.; Sumpter, B. G.; Meunier, V. Ion Distribution in Electrified Micropores and Its Role in the Anomalous Enhancement of Capacitance. *ACS Nano* **2010**, *4*, 2382–2390.
- (52) Vatamanu, J.; Borodin, O.; Smith, G. D. Molecular Simulations of the Electric Double Layer Structure, Differential Capacitance, and Charging Kinetics for *N*-Methyl-*N*-propylpyrrolidinium Bis-(fluorosulfonyl)imide at Graphite Electrodes. *J. Phys. Chem. B* **2011**, *115*, 3073–3084.
- (53) Singh, R.; Monk, J.; Hung, F. R. Heterogeneity in the Dynamics of the Ionic Liquid [BMIM⁺][PF₆[−]] Confined in a Slit Nanopore. *J. Phys. Chem. C* **2011**, *115*, 16544–16554.
- (54) Vatamanu, J.; Borodin, O.; Smith, G. D. Molecular Insights into the Potential and Temperature Dependences of the Differential Capacitance of a Room-Temperature Ionic Liquid at Graphite Electrodes. *J. Am. Chem. Soc.* **2010**, *132*, 14825–14833.
- (55) Rajput, N. N.; Monk, J.; Singh, R.; Hung, F. R. On the Influence of Pore Size and Pore Loading on Structural and Dynamical Heterogeneities of an Ionic Liquid Confined in a Slit Nanopore. *J. Phys. Chem. C* **2012**, *116*, 5170–5182.
- (56) Rajput, N. N.; Monk, J.; Hung, F. R. Structure and Dynamics of an Ionic Liquid Confined Inside a Charged Slit Graphitic Nanopore. *J. Phys. Chem. C* **2012**, *116*, 14504–14513.
- (57) Jiang, D. E.; Jin, Z. H.; Henderson, D.; Wu, J. Z. Solvent Effect on the Pore-Size Dependence of an Organic Electrolyte Supercapacitor. *J. Phys. Chem. Lett.* **2012**, *3*, 1727–1731.
- (58) Shim, Y.; Jung, Y.; Kim, H. J. Graphene-Based Supercapacitors: A Computer Simulation Study. *J. Phys. Chem. C* **2011**, *115*, 23574–23583.
- (59) Vatamanu, J.; Borodin, O.; Bedrov, D.; Smith, G. D. Molecular Dynamics Simulation Study of the Interfacial Structure and Differential Capacitance of Alkylimidazolium Bis(trifluoromethanesulfonyl)imide [C_nmim][TFSI] Ionic Liquids at Graphite Electrodes. *J. Phys. Chem. C* **2012**, *116*, 7940–7951.

- (60) Vatamanu, J.; Borodin, O.; Smith, G. D. Molecular Dynamics Simulations of Atomically Flat and Nanoporous Electrodes with a Molten Salt Electrolyte. *Phys. Chem. Chem. Phys.* **2010**, *12*, 170–182.
- (61) Feng, G. A.; Qiao, R.; Huang, J. S.; Dai, S.; Sumpster, B. G.; Meunier, V. The Importance of Ion Size and Electrode Curvature on Electrical Double Layers in Ionic Liquids. *Phys. Chem. Chem. Phys.* **2011**, *13*, 1152–1161.
- (62) Huang, J. S.; Qiao, R.; Sumpster, B. G.; Meunier, V. Effect of Diffuse Layer and Pore Shapes in Mesoporous Carbon Supercapacitors. *J. Mater. Res.* **2010**, *25*, 1469–1475.
- (63) Shim, Y.; Kim, H. J. Nanoporous Carbon Supercapacitors in an Ionic Liquid: A Computer Simulation Study. *ACS Nano* **2010**, *4*, 2345–2355.
- (64) Shim, Y.; Kim, H. J. Solvation of Carbon Nanotubes in a Room-Temperature Ionic Liquid. *ACS Nano* **2009**, *3*, 1693–1702.
- (65) Dong, K.; Zhou, G.; Liu, X.; Yao, X.; Zhang, S.; Lyubartsev, A. Structural Evidence for the Ordered Crystallites of Ionic Liquid in Confined Carbon Nanotubes. *J. Phys. Chem. C* **2009**, *113*, 10013–10020.
- (66) Singh, R.; Monk, J.; Hung, F. R. A Computational Study of the Behavior of the Ionic Liquid [BMIM⁺][PF₆[−]] Confined inside Multiwalled Carbon Nanotubes. *J. Phys. Chem. C* **2010**, *114*, 15478–15485.
- (67) Coasne, B.; Viau, L.; Vioux, A. Loading-Controlled Stiffening in Nanoconfined Ionic Liquids. *J. Phys. Chem. Lett.* **2011**, *2*, 1150–1154.
- (68) Yang, L.; Fishbine, B. H.; Migliori, A.; Pratt, L. R. Molecular Simulation of Electric Double-Layer Capacitors Based on Carbon Nanotube Forests. *J. Am. Chem. Soc.* **2009**, *131*, 12373–12376.
- (69) Jiang, D. E.; Wu, J. Z. Microscopic Insights into the Electrochemical Behavior of Nonaqueous Electrolytes in Electric Double-Layer Capacitors. *J. Phys. Chem. Lett.* **2013**, *4*, 1260–1267.
- (70) Feng, G.; Li, S.; Atchison, J. S.; Presser, V.; Cummings, P. T. Molecular Insights into Carbon Nanotube Supercapacitors: Capacitance Independent of Voltage and Temperature. *J. Phys. Chem. C* **2013**, *117*, 9178–9186.
- (71) Kondrat, S.; Perez, C. R.; Presser, V.; Gogotsi, Y.; Kornyshev, A. A. Effect of Pore Size and Its Dispersity on the Energy Storage in Nanoporous Supercapacitors. *Energy Environ. Sci.* **2012**, *5*, 6474–6479.
- (72) Merlet, C.; Salanne, M.; Rotenberg, B.; Madden, P. A. Influence of Solvation on the Structural and Capacitive Properties of Electrical Double Layer Capacitors. *Electrochim. Acta* **2013**, *101*, 262–271.
- (73) Singh, R.; Rajput, N. N.; He, X.; Monk, J.; Hung, F. R. Molecular Dynamics Simulations of the Ionic Liquid [EMIM⁺][TFMSI[−]] Confined Inside Rutile (110) Slit Nanopores. *Phys. Chem. Chem. Phys.* **2013**, *15*, 16090–16103.
- (74) Vatamanu, J.; Cao, L. L.; Borodin, O.; Bedrov, D.; Smith, G. D. On the Influence of Surface Topography on the Electric Double Layer Structure and Differential Capacitance of Graphite/Ionic Liquid Interfaces. *J. Phys. Chem. Lett.* **2011**, *2*, 2267–2272.
- (75) Xing, L. D.; Vatamanu, J.; Smith, G. D.; Bedrov, D. Nanopatterning of Electrode Surfaces as a Potential Route To Improve the Energy Density of Electric Double-Layer Capacitors: Insight from Molecular Simulations. *J. Phys. Chem. Lett.* **2012**, *3*, 1124–1129.
- (76) Merlet, C.; Rotenberg, B.; Madden, P. A.; Taberna, P. L.; Simon, P.; Gogotsi, Y.; Salanne, M. On the Molecular Origin of Supercapacitance in Nanoporous Carbon Electrodes. *Nat. Mater.* **2012**, *11*, 306–310.
- (77) Merlet, C.; Péan, C.; Rotenberg, B.; Madden, P. A.; Simon, P.; Salanne, M. Simulating Supercapacitors: Can We Model Electrodes as Constant Charge Surfaces? *J. Phys. Chem. Lett.* **2012**, *4*, 264–268.
- (78) Vatamanu, J.; Borodin, O.; Bedrov, D.; Smith, G. D. Molecular Dynamics Simulation Study of the Interfacial Structure and Differential Capacitance of Alkylimidazolium Bis(trifluoromethanesulfonyl)imide [C_nmim][TFSI] Ionic Liquids at Graphite Electrodes. *J. Phys. Chem. C* **2012**, *116*, 7940–7951.
- (79) Monk, J.; Singh, R.; Hung, F. R. Effects of Pore Size and Pore Loading on the Properties of Ionic Liquids Confined Inside Nanoporous CMK-3 Carbon Materials. *J. Phys. Chem. C* **2011**, *115*, 3034–3042.
- (80) Feng, G.; Jiang, D.-e.; Cummings, P. T. Curvature Effect on the Capacitance of Electric Double Layers at Ionic Liquid/Onion-Like Carbon Interfaces. *J. Chem. Theory Comput.* **2012**, *8*, 1058–1063.
- (81) Li, S.; Feng, G.; Fulvio, P. F.; Hillesheim, P. C.; Liao, C.; Dai, S.; Cummings, P. T. Molecular Dynamics Simulation Study of the Capacitive Performance of a Binary Mixture of Ionic Liquids near an Onion-like Carbon Electrode. *J. Phys. Chem. Lett.* **2012**, *3*, 2465–2469.
- (82) Palmer, J. C.; Moore, J. D.; Brennan, J. K.; Gubbins, K. E. Simulating Local Adsorption Isotherms in Structurally Complex Porous Materials: A Direct Assessment of the Slit Pore Model. *J. Phys. Chem. Lett.* **2011**, *2*, 165–169.
- (83) Pikunic, J.; Pellenc, R. J. M.; Thomson, K. T.; Rouzaud, J. N.; Levitz, P.; Gubbins, K. E. Improved Molecular Models for Porous Carbons. In *Studies in Surface Science and Catalysis*; Yasuhiro Iwasawa, N. O., Hironobu, K., Eds.; Elsevier: New York, 2001; Vol. 132; pp 647–652.
- (84) Turner, C. H.; Pikunic, J.; Gubbins, K. E. Influence of Chemical and Physical Surface Heterogeneity on Chemical Reaction Equilibria in Carbon Micropores. *Mol. Phys.* **2001**, *99*, 1991–2001.
- (85) Hess, B.; Kutzner, C.; van der Spoel, D.; Lindahl, E. GROMACS 4: Algorithms for Highly Efficient, Load-Balanced, and Scalable Molecular Simulation. *J. Chem. Theory Comput.* **2008**, *4*, 435–447.
- (86) Kelkar, M. S.; Maginn, E. J. Effect of Temperature and Water Content on the Shear Viscosity of the Ionic Liquid 1-Ethyl-3-methylimidazolium Bis(trifluoromethanesulfonyl)imide As Studied by Atomistic Simulations. *J. Phys. Chem. B* **2007**, *111*, 4867–4876.
- (87) Thomson, K. T.; Gubbins, K. E. Modeling Structural Morphology of Microporous Carbons by Reverse Monte Carlo. *Langmuir* **2000**, *16*, 5761–5773.
- (88) Gelb, L. D.; Gubbins, K. E. Pore Size Distributions in Porous Glasses: A Computer Simulation Study. *Langmuir* **1998**, *15*, 305–308.
- (89) Palmer, J. C.; Llobet, A.; Yeon, S. H.; Fischer, J. E.; Shi, Y.; Gogotsi, Y.; Gubbins, K. E. Modeling the Structural Evolution of Carbide-Derived Carbons Using Quenched Molecular Dynamics. *Carbon* **2010**, *48*, 1116–1123.
- (90) Fredlake, C. P.; Crosthwaite, J. M.; Hert, D. G.; Aki, S.; Brennecke, J. F. Thermophysical Properties of Imidazolium-Based Ionic Liquids. *J. Chem. Eng. Data* **2004**, *49*, 954–964.
- (91) Bussi, G.; Donadio, D.; Parrinello, M. Canonical Sampling through Velocity Rescaling. *J. Chem. Phys.* **2007**, *126*, 014101.
- (92) Bussi, G.; Zykova-Timan, T.; Parrinello, M. Isothermal-Isobaric Molecular Dynamics Using Stochastic Velocity Rescaling. *J. Chem. Phys.* **2009**, *130*, 074101.
- (93) Porter, A. R.; Liem, S. Y.; Popelier, P. L. A. Room Temperature Ionic Liquids Containing Low Water Concentrations-A Molecular Dynamics Study. *Phys. Chem. Chem. Phys.* **2008**, *10*, 4240–4248.
- (94) Tsuzuki, S.; Shinoda, W.; Saito, H.; Mikami, M.; Tokuda, H.; Watanabe, M. Molecular Dynamics Simulations of Ionic Liquids: Cation and Anion Dependence of Self-Diffusion Coefficients of Ions. *J. Phys. Chem. B* **2009**, *113*, 10641–10649.
- (95) Hu, Z. H.; Margulis, C. J. Heterogeneity in a Room-Temperature Ionic Liquid: Persistent Local Environments and the Red-Edge Effect. *Proc. Natl. Acad. Sci. U.S.A.* **2006**, *103*, 831–836.